Afyon Kocatepe Üniversitesi Fen ve Mühendislik Bilimleri Dergisi
Afyon Kocatepe University – Journal of Science and Engineering
https://dergipark.org.tr/tr/pub/akufemubid

Araştırma Makalesi / Research Article
e-ISSN: 2149-3367
DOI: https://doi.org/10.35414/akufemubid.1969024
CITE: Afyon Kocatepe University Journal of Science and Engineering. 26(5) (2026) 1167-1185

Kinetics, Isotherm, and Thermodynamics of Reactive Yellow RR Adsorption on Pineapple-Derived Activated Carbon

*Makale Bilgisi / Article Info
Alındı/Received: 11.06.2026
Kabul/Accepted: 17.09.2026
Yayımlandı/Published: 06.10.2026

Ananas Kabuğundan Üretilen Aktif Karbon Kullanılarak Reaktif Yellow RR Boyasının Adsorpsiyonu: Kinetik, İzoterm ve Termodinamik Analiz

Selen YAKAR[1*], Unsal ACIKEL[1], Leyla Durmazucar[1], Handan YAKAR[2]

[1]*Cumhuriyet Üniversitesi, Mühendislik Fakültesi, Kimya Mühendisliği Bölümü, Sivas, Türkiye*
[2]*Dokuz Eylül Üniversitesi, Teknoloji Fakültesi, Otomotiv Mühendisliği Bölümü, Izmir, Türkiye*

© 2026 The Authors | Creative Commons Attribution-Noncommercial 4.0 (CC BY-NC) International License

Abstract

Reactive dyes are a harmful substance found in large quantities in wastewater, posing a significant environmental threat. Activated carbon is often preferred for purification wastewater and recent research has explored sustainable production methods using natural precursors. In this research, activated carbon was synthesized from pineapple peel (coded PP) using K_2CO_3. Different ratios (1/1, 2/1, 3/1) and chemical activation temperatures (400-600 °C) were applied for durations of 1, 2, and 3 hours. The most efficient activated carbon sample (coded AC60032) was produced at a 2/1 ratio, 600 °C, for 3 hours, yielding a surface area of 1244.09 m^2/g. Characterization was conducted using BET, SEM, FTIR, XRD, and TGA analyses. The adsorption capacity of Yellow RR dye was assessed under different conditions: pH (2–6), dye concentration (20–100 mg/L), contact time (60–240 min), adsorbent dosage (1–4 g), temperature (20–50 °C), and stirring speed (100–250 rpm). The adsorption process fitted the Freundlich isotherm model (R^2 = 0.99) and was determined to be endothermic, with a maximum adsorption capacity of 105.02 mg/g at 323 K. These findings highlight the potential of pineapple peel-derived activated carbon as an effective and sustainable adsorbent for removing reactive dyes from wastewater.

Keywords: *Biomass active carbon; Adsorption; Sustainability; Textile dye; Wastewater treatment*

Öz

Reaktif boyar maddeler, atıksularda yüksek miktarlarda bulunan ve çevre için önemli bir kirlilik kaynağı oluşturan zararlı bileşiklerdir. Bu çalışmada, atıksu arıtımında yaygın olarak kullanılan aktif karbonun sürdürülebilir üretimi amacıyla ananas kabuğu (PP) hammadde olarak seçilmiştir. K_2CO_3 kullanılarak kimyasal aktivasyon gerçekleştirilmiş; 1/1, 2/1 ve 3/1 oranlarında impregnasyon, 400–600 °C karbonizasyon sıcaklıklarında ve 1, 2 ve 3 saat sürelerde uygulanmıştır. En yüksek performans gösteren AC60032 numunesi, 2/1 K_2CO_3/PP oranında, 600 °C'de 3 saat karbonizasyon ile elde edilmiş ve 1244,09 m^2/g yüzey alanına ulaşmıştır. Elde edilen aktif karbonlar BET, SEM, FTIR, XRD ve TGA analizleri ile karakterize edilmiştir. Yellow RR boyar maddesinin adsorpsiyon performansı; pH (2–6), başlangıç derişimi (20–100 mg/L), temas süresi (60–240 dk), adsorban dozajı (1–4 g), sıcaklık (20–50 °C) ve karıştırma hızı (100–250 rpm) gibi farklı çalışma koşullarında incelenmiştir. Adsorpsiyon sürecinin Freundlich izoterm modeline uygun olduğu (R^2 = 0,99) ve endotermik karakter gösterdiği belirlenmiştir. Ayrıca 323 K'de maksimum adsorpsiyon kapasitesi 105.02 mg/g olarak hesaplanmıştır. Bu sonuçlar, ananas kabuğundan elde edilen aktif karbonun reaktif boyar maddelerin gideriminde etkili ve sürdürülebilir bir adsorban olduğunu göstermektedir.

Anahtar Kelimeler: *Biyokütle kaynaklı aktif karbon; Adsorpsiyon, Sürdürülebilirlik; Tekstil boyası; Atıksu arıtımı*

1. Introduction

The expansion of industrial activities has increased pressure on water resources, with textile manufacturing contributing substantially through intensive water and chemical use and the release of dye-laden effluents into aquatic environments. (Teweldebrihan et *al.* 2024, Slama et *al.* 2021, Liu et *al.* 2024).

Reactive dyes are of particular concern due to their low fixation efficiency, high water solubility, and chemical stability, resulting in persistent dye contamination in wastewater (Ledakowicz et *al.* 2021, Lykidou et *al.* 2023). Among various treatment methods, adsorption has gained attention as an effective approach due to its simplicity, cost-effectiveness, and environmental compatibility (Dutta et al. 2021; Aragaw and Bogale 2021).

The success of the adsorption process depends largely on the adsorbent material. Porous materials, especially those derived from low-cost biomass, have shown promising performance in dye removal applications (Yadav et *al.* 2024, Li et *al.* 2022). Among these, activated carbon is widely used owing to its porous structure and

*Sorumlu Yazar/Corresponding Author: Selen YAKAR e-posta/e-mail: selenyakar@cumhuriyet.edu.tr

abundant adsorption sites. (Lawtae et *al*. 2021, Li et *al*. 2023). For example, activated carbon produced from fox nutshells showed a surface area of 2408.9 m^2/g and remarkable adsorption capacity for malachite green (Srivastava et *al*. 2025).

Agricultural wastes are increasingly explored as low-cost precursors for activated carbon. Pineapple peel is a promising feedstock, although studies have mainly employed KOH or physical activation. The use of K_2CO_3-activated pineapple peel carbon for Reactive Yellow RR removal remains largely unexplored.

This study developed K_2CO_3-activated carbon from waste pineapple peel for Reactive Yellow RR removal. Its adsorption behaviour was assessed using kinetic, equilibrium, thermodynamic, and intraparticle diffusion models. The resulting activated carbon (AC60032) showed a BET surface area of ~1244 m^2/g, highlighting pineapple peel as a viable precursor for high-performance adsorbents.

2. Materials and Methods

2.1. Chemicals

Chemical substances required for this research were supplied by Kimyalab. KIMYALAB Potassium Carbonate (Granular), KIMYALAB 0.1N HCl, KIMYALAB 0.1N NaOH. H_2SO_4 (98% extra pure) were used by making the necessary dilutions.

Reactive Yellow RR (Remazol® Yellow RR gran) was supplied by DyStar, Germany and used as the model adsorbate without further purification. The dye is a commercial vinyl sulfone-type reactive dye supplied in granular powder form with 100% strength. According to the manufacturer's technical data sheet, the dye exhibits a neutral solubility of 100 g L^{-1} without salt and a fixation value of approximately 80% under the cold pad-batch process.

2.2 Activated carbon production from pineapple peel

In this study, K_2CO_3-activated carbon derived from pineapple peel was used to remove Yellow RR from aqueous solution. Similar agricultural waste-based adsorbents have shown effective dye removal in recent studies (Zayed et *al.* 2023, Mamatha 2023).

Pineapple peels were collected from supermarkets, washed, and oven-dried at 90 °C for 24 h. The dried material was ground, sieved (<350 µm), washed twice with purified water, and dried at 80 °C for a further 24 h. It was then milled to 0–350 µm before K_2CO_3 activation.

Raw material and K_2CO_3 were mixed in the ratios of 1/1, 1/2, 1/3 (g raw material/g K_2CO_3). For each mixture, 700 mL of water was added to form a mud-like consistency. The mixtures were heated at 70 °C for 3 h with occasional stirring, followed by 21 h at room temperature with intermittent stirring. They were then filtered, transferred to glass jars, and dried at 90 °C for 24 h.

Previous studies indicate that hemicellulose and cellulose in pineapple peel mainly decompose below 350 °C, while lignin degradation and volatile matter removal extend to approximately 600 °C (Sanni et al., 2025). Based on this thermal behaviour and the TG-DTG results, an activation range of 400–600 °C was selected in this study. Although K_2CO_3 activation is commonly performed at temperatures around 800 °C, effective activation at lower temperatures has also been reported. Foo and Hameed (2012) investigated chemically activated carbon derived from pineapple peel, while Zhu et al. (2018) and Sahu et al. (2023) demonstrated that K_2CO_3 activation can be effective at 400-600 °C.

The dried samples were brought to 0-350 µm grain and placed in steel containers with lids having two holes on them and chemically activated for 1, 2 and 3 hours at 400°C, 500°C, 600°C, under a nitrogen atmosphere with a heating rate of 10 °C min^{-1}. After chemical activation, the activated carbons were washed with distilled water and 200 mL of 0.1 M HCl. Washing was repeated until the filtrate reached pH 6–7, indicating effective removal of residual activating chemicals. $AgNO_3$ testing can also be employed as a complementary analytical method for confirming chloride removal and evaluating the purification efficiency after HCl washing. The washed samples were placed in covered porcelain containers and dried in the drying-oven at 90°C for 24 hours. The dried activated carbons were sieved to 0-109 µm grain size. Pineapple peel and activated carbon were subjected to FTIR, SEM, BET, TGA, XRD characterization tests.

A 1000 mg/L Yellow RR stock solution was prepared using purified water for the adsorption experiments.

During K_2CO_3-assisted activation, both the thermal decomposition of pineapple peel and its interaction with K_2CO_3 influence carbon development. At around 400 °C, hemicellulose and cellulose decomposition promotes carbon formation, while K_2CO_3 begins reacting with oxygen-containing groups. At 500–600 °C, further lignin decomposition and carbonization occur, with potassium-containing species contributing to carbon rearrangement and pore development. Therefore, the selected temperature range (400–600 °C) allows the combined effects of biomass decomposition and K_2CO_3 activation on activated carbon development to be evaluated (Zhu et *al.* 2018, Sahu et *al.* 2023, Sanni et *al.* 2025)

2.3 Characterization of materials

Elemental analysis was carried out with Thermo Flash 2000 device. Proximate analysis was conducted by using NÜVE FN 500 brand drying-oven and MAGMATHERM MT 1100-5-U8-SW brand muffle furnace. Brunauer-Emmett-Teller (BET) analysis was performed with Quantachrome /NOVA Touch LX4 device at 77.35 K by adsorption-desorption process of N_2 gas. X-Ray Diffraction (XRD) analyses were determined with Panalytical /Empyrean device. Fourier Transform Infrared (FT-IR) spectrum analysis was conducted with Bruker Tensor II device. Scanning Electron Microscopy (SEM) analysis was conducted with TESCAN MIRA3 XMU device. Yellow RR aqueous solution concentration measurements were performed with UV-Vis Spectrometer Shımadzu (1201-V) device.

2.4.Yellow RR adsorption *with AC60032*

A batch adsorption system was used in this study. Briefly, 100 mL of Yellow RR dye solution was mixed with 1 g L^{-1} of AC60032 (BET surface area: 1244.09 m^2 g^{-1}) in 250 mL conical flasks. The mixtures were agitated at 200 rpm using a heated shaker (IKA-WERKE RT 10 POWER) at 293 K. The effect of AC60032 on Yellow RR removal was investigated under different experimental conditions, including pH (2-6), adsorbent amount (1-4 g), initial dye concentration (20-100 mg L^{-1}), temperature (20-50 °C), contact time (60-240 min), and stirring speed (100-250 rpm). During the experiments, 5 mL samples were withdrawn at hourly intervals and centrifuged at 4000 rpm for 15 min. After separation of AC60032, the supernatant was analyzed at the maximum absorption wavelength (λ = 415 nm) using a UV–Vis spectrophotometer. All adsorption experiments were repeated to verify the reproducibility of the results. The close agreement among the replicate measurements confirmed the consistency of the experimental data.

To quantify equilibrium adsorption qe(mg/g), was computed via equation presented below.

$$q_e = \frac{[(C_0 - C_e)xV]}{W} \quad (1)$$

Here, q_e(mg/g) refers the quantity of Yellow RR retained at equilibrium per gram of activated carbon. C_0 and C_e(mg/L) correspond to the initial and equilibrium dye concentrations for Yellow RR, m is the weight of activated carbonused, V is thevolume (L) of solution.

Yield of adsorbed dye (Ads %) yield (de Farias Silva et al. 2020; Alamzeb et al. 2022),

$$Ads\% = \left(\frac{C_0 - C_e}{C_0}\right) x100 \quad (2)$$

2.5 Adsorption isotherm and kinetic modelling

The adsorption equilibrium data were analyzed using Langmuir and Freundlich isotherm models, while adsorption kinetics were evaluated using pseudo-first-order, pseudo-second-order, Elovich, and intraparticle diffusion (Weber–Morris) models. The equations of the applied models are presented in Table 1. Model parameters were determined based on the experimental adsorption data.

Table 1. Adsorption isotherm and kinetic models

Model	Equation
Langmuir isotherm	$q_e = \frac{q_{max} K_L C_e}{1 + K_L C_e}$
Freundlich isotherm	$q_e = K_F C_e^{1/n}$
Pseudo-first-order model	$q_t = q_e(1 - e^{-k_1 t})$
Pseudo-second-order model	$q_t = \frac{k_2 q_e^2 t}{1 + k_2 q_e t}$
Elovich model	$q_t = \frac{1}{\beta} \ln(1 + \alpha\beta t)$
Intraparticle diffusion model (Weber–Morris)	$q_t = k_{id} t^{1/2} + C$

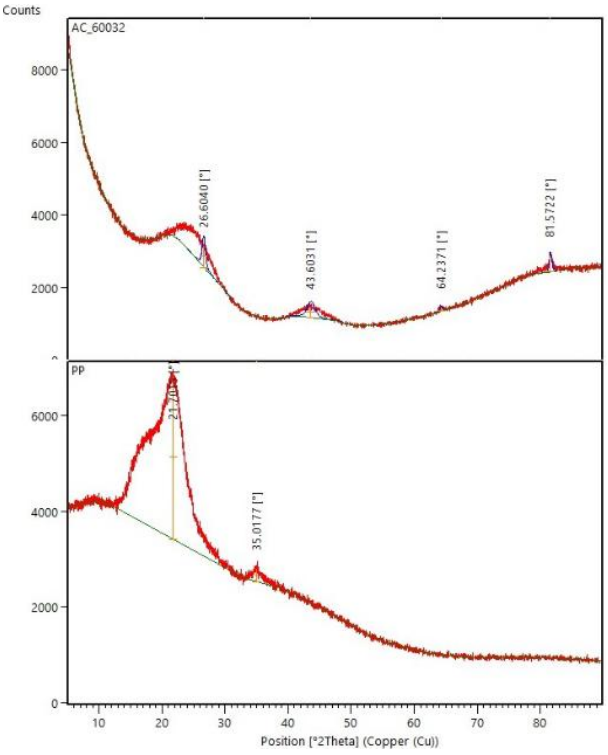


Figure 1. XRD analysis of a. AC60032 and b. PP

3. Results and Discussions

3.1. XRD (X-Ray Diffraction Analysis)

XRD is an important technique that enables the characterization of the changed structure (Wang et *al.* 2022). PP XRD graph in Figure 1(b) exhibited diffraction peaks at approximately 2θ = 21.69° and 35.02°. The peak at 2θ = 21.69° can be attributed to the crystalline

components present in the lignocellulosic structure of pineapple peel, while the weaker peak at 2θ = 35.02° may be related to mineral components and other carbon-containing structures.The XRD analysis of AC60032 in Figure 1(a) reveals two diffraction peaks, one at approximately 2θ = 24° and 44°, corresponding to the (002) and (100) planes of turbostratic carbon structures, respectively (Anusonthiwong et *al.* 2025).

In XRD analysis, the absence of clear and sharp peaks indicates that the material has an amorphous structure. This indicates that the pineapple peel has gained an irregular structure instead of a regular crystalline structure during the chemical activation process.

Amorphous carbon offers a porous structure and is ideal for the adsorption properties required in activated carbon.

3.2. TG-DTG (Differential Thermogravimetric Analysis)

At Figure 2 Lignocellulosic masses can decompose under varying thermal conditions, hemicellulose at 180-290°C, cellulose at 240-350°C and lignin at 280-500°C (El-Sayed et *al.* 2024). In the analysis where a heating rate of less than 100 °C/min was applied, the thermal decomposition process of biomass occurs in four different steps. These steps were moisture removal, hemicellulose degradation, cellulose degradation and lignin degradation, respectively (Pérez et *al.* 2025)

At Figure 3 a small reduction in mass is detected up to 200°C. It results from the release of physically bound water molecules from the AC60032. There is a mass loss of 74% between 400-600°C. This temperature range indicates indicating the decomposition of remaining organic components and the development of the carbon structure. These thermal degradation characteristics support the selection of the 400-600 °C activation temperature range used in this study. While 60% mass loss is observed up to 400°C in pp, it is around 10% in AC60032. This is also due to the better thermal resistance of AC60032 due to the K+ metal ion in the structure of K_2CO_3 used as the activating agent (Petri et *al.* 2025).

At 600°C and above, the mass loss is less and approaches a constant level. This shows that the carbon has become more stable and the remaining substance is fixed carbon. The 34% decrease after 900°C shows that the carbon structure can be further deteriorated and become thermally unstable.

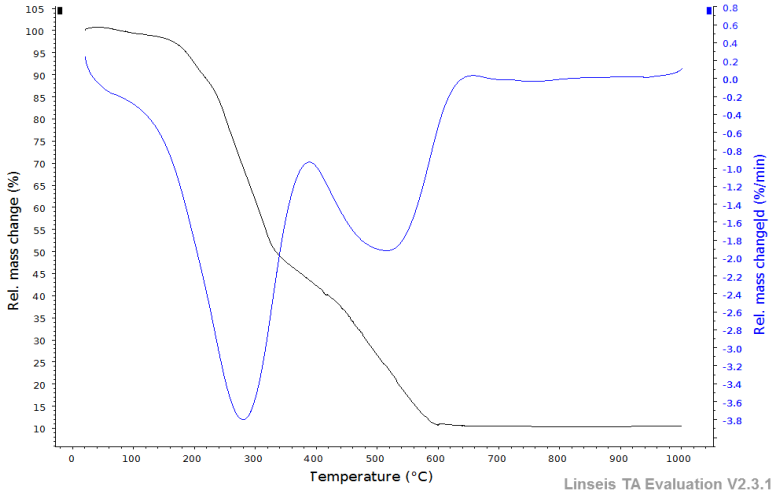


Figure 2. TG-DTG analysis of PP

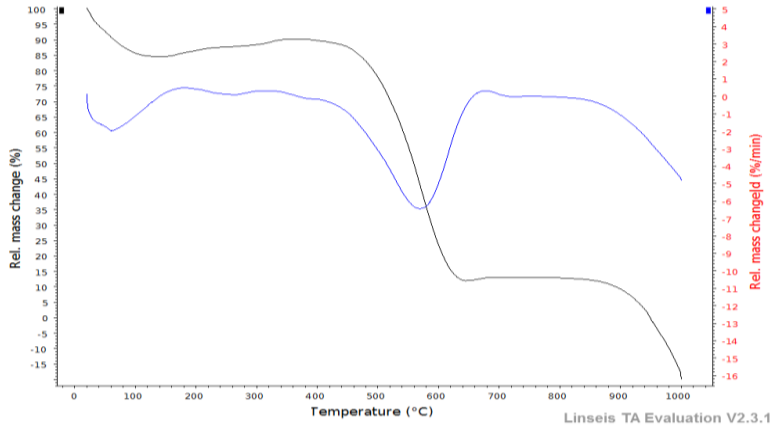


Figure 3. TG-DTG analysis of AC60032

3.3. FTIR (Fourier Transform Infrared Spectroscopy)

FTIR analyses were investigated to determine and compare the surface functional groups of pineapple peel, AC60032 and Yellow RR after adsorption.

Upon examination of the PP spectrum, broad band detected in the wavelength range of 3600-3300 cm^{-1} originates from hydroxyl compounds containing intense hydrogen bonds (Duraisamy et al. 2025). In the 2916-2850 cm-1 band range, it is due to the asymmetric and symmetric –C-H stretching of aliphatic methyl (-CH3) and methylene (-CH2) functional groups (Mosaffa et al. 2024) The stretching band observed at 1730.75 cm^{-1} originates from the C=O groups found in the ester, aldehyde, ketone and acetyl derivatives in the structure (Li et al. 2022). The sharp band appearing at 1034.01 cm^{-1} is associated with C-O and C-C vibration in alkanes, alcohols, phenols, ethers, and lipids (Ulpathakumbura et al. 2023).

The bands seen at 1077.68, 1136.84 cm^{-1} originate from C-O stretching vibrations in carboxylic acids, alcohols, phenols, and esters present in possible structures (Jesus et al. 2024). A weaker OH band is observed around 3643 cm^{-1} in the spectrum of AC60032. It is thought to be related to the reduction of OH group, thermal decomposition and loss of oxygenated functional groups on the surface. The strong C-H peak observed at 2917.35 in Pineapple peel has transformed into weaker C-H peaks in the range of 2980-2872 cm^{-1} in AK60032. Aliphatic C-H bonds have largely disappeared. This shows that volatile organic compounds are removed during pyrolysis and the structure becomes more graphitic.

The aromatic weak C=C peaks at 1517 cm^{-1} and 1421 cm^{-1} have transformed into a strong C=C bond around 1571 cm^{-1} in AC60032. Similarly, it was determined that the absorption band of the υ(C=O) double bond at 1730.75 cm-1 in the PP spectrum was not seen in the AC60032 spectrum. After chemical activation, it became evident that the oxygen-containing aromatic and aliphatic surface functional groups of the PP samples were broken down and new structures were formed. In the spectrum, absorption peaks at wavelengths of 2800-2000 cm^{-1}, which were not seen, stand out in the AC60032 spectrum (Hafizah et al. 2025). –OH and -NH vibrations are observed between 3200cm^{-1} and 3500cm^{-1} wavelengths.

The sharpening of the peaks at 1136.88 cm^{-1} and 1028.68 cm^{-1} in the spectrum after adsorption may suggest the presence of sulfonate ($-SO_3^-$) or sulfate ($-SO_4^{2-}$) groups in the reactive dye. The peak at 573 cm^{-1} may probably correspond to the S-O single bond vibration or metal-sulfate interactions. The observation of the peak at 870.01 cm^{-1} associated with the C-H outer plane bending vibrations of aromatic rings or some sulfate ($-SO_4$) and phosphate ($-PO_4$) groups supports the adsorption of the dye (Thamer et al. 2023).

Figure 4 presents the FTIR spectra of PP before and after adsorption into AC60032, highlighting the changes in functional groups involved in the adsorption process. These spectral changes indicate the interaction between Yellow RR molecules and the surface functional groups of AC60032. The adsorption mechanism may involve hydrogen bonding and electrostatic interactions between the dye molecules and oxygen-containing functional groups on the AC60032 surface.

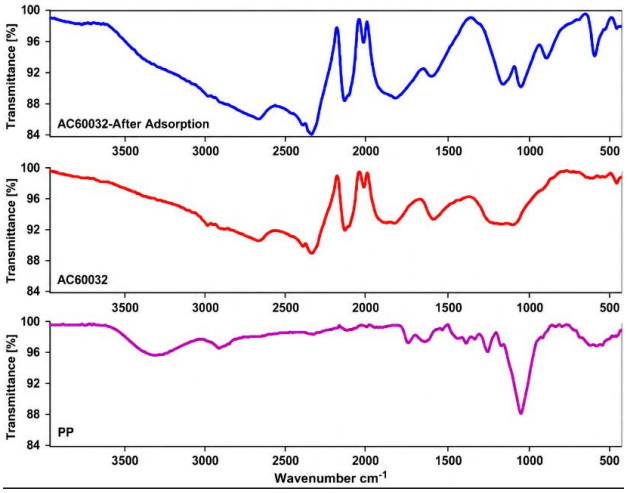


Figure 4. FTIR analysis PP, before and after adsorption AC60032

3.4. SEM (Scanning Electron Microscope) analysis

The SEM image of pineapple peel revealed its natural porous structure, indicating its suitability as a precursor for activated carbon production (Gan 2021). The SEM image of AC60032 showed a developed porous surface structure formed during K_2CO_3-assisted chemical activation due to the release of volatile compounds and structural rearrangement of the carbon matrix (Illingworth et *al*. 2022). The absence of severe structural collapse indicates the preservation of the porous framework. Thermal stability was evaluated separately by TG–DTG analysis.

After Yellow RR adsorption, partial pore blocking, surface coating, and dye-related deposits were observed in the SEM image (Figure 5), confirming the successful interaction between Yellow RR molecules and AC60032.

3.5. BET (Brunauer-Emmett-Teller) analysis

To produce AC60032, pineapple peel was chemically activated with K_2CO_3 at different impregnation ratios (K_2CO_3/pineapple peel = 1/1, 2/1, and 3/1 by mass) and activation temperatures (400, 500, and 600 °C). The BET surface areas of the obtained samples were measured,

and the results are presented in Table 1. The outcomes show that as the temperature increases, there is a notable enhancement in surface area (Tsai et *al*. 2023, Liu et *al.* 2024). Among the prepared activated carbons, AC60032, produced using a K_2CO_3/pineapple peel ratio of 2/1 at 600 °C, exhibited the highest BET surface area of 1244.09 m^2/g, compared with 26 m^2/g for untreated pineapple peel. Based on the BET results and SEM observations, AC60032 was selected for the subsequent adsorption experiments. Table 2 shows the surface areas (m^2/g) of activated carbon samples produced with different chemical activation temperatures, times and chemical activation rates. An increase in surface areas was observed as the temperature increased (Karume et *al*. 2023, Kundu et *al.* 2024). While the treatment rates showed different reactions at different temperatures, the greatest BET surface area (1275 m^2/g) was obtained in AC60031 with 1/1 K_2CO_3/pineapple peel ratio, it was observed that 1/1 K_2CO_3/pineapple peel ratio caused foaming in the materials. To keep the material's structure intact and ensure the production process remains controllable, AC60032 (1244.09 m^2/g) obtained in 3 hours at 600 ℃ with 2/1 treatment ratio was selected as the adsorbent. The BET surface area of AC60032 (1244.09 m^2/g) was compared with previously reported pineapple peel-derived activated carbons. Foo and Hameed (2012) reported a BET surface area of 1160 m^2/g for pineapple peel-based activated carbon prepared using KOH activation, while Tsai et al. (2023) obtained surface areas in the range of 569.56–843.09 m^2/g using CO_2 activation and post-treatment processes. The higher surface area obtained for AC60032 indicates that the selected K_2CO_3 activation conditions effectively promoted pore development and resulted in a highly porous carbon structure suitable for adsorption applications.

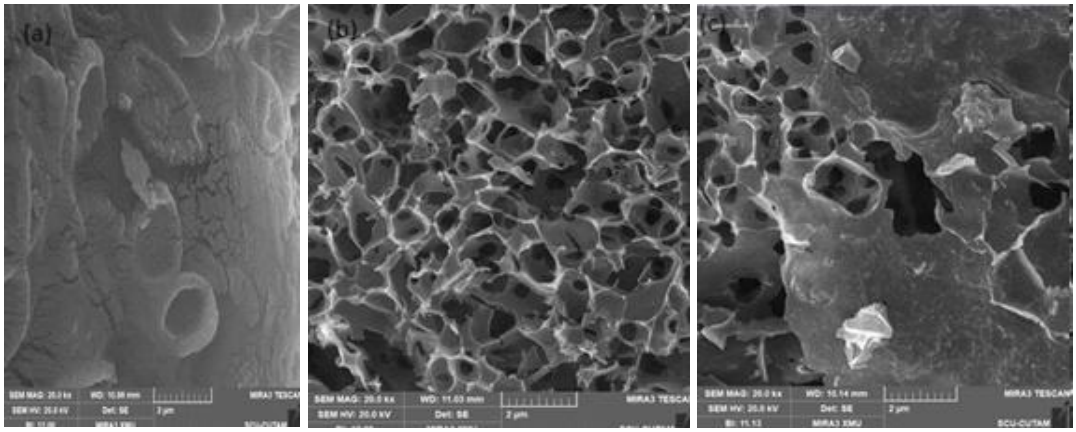


Figure 5. SEM Images of (a) PP, (b) AC60032 before adsorption, (c) AC60032 after adsorption

Table 2. BET-based surface analysis of activated carbons

Sample Code	Chemical Activation Temperature	Chemical Activation Time	K2CO3/PP treating rate	Surface Area (m^2/g)
AC40011	400 °C	1h	1/1	62,28
AC40012	400 °C	1h	2/1	365,31
AC40013	400 °C	1h	3/1	131,55
AC40021	400 °C	2h	1/1	78,83
AC40022	400 °C	2h	2/1	156,20
AC40023	400 °C	2h	3/1	133,64
AC40031	400 °C	3h	1/1	152,18
AC40032	400 °C	3h	2/1	446,22
AC40033	400 °C	3h	3/1	221,85
AC50011	500 °C	1h	1/1	521,67
AC50012	500 °C	1h	2/1	532,72
AC50013	500 °C	1h	3/1	534,94
AC50021	500 °C	2h	1/1	574,96
AC50022	500 °C	2h	2/1	468,91
AC50023	500 °C	2h	3/1	460,46
AC50031	500 °C	3h	1/1	460,63
AC50032	500 °C	3h	2/1	452,34
AC50033	500 °C	3h	3/1	432,93
AC60011	600 °C	1h	1/1	1221
AC60012	600 °C	1h	2/1	889,31
AC60013	600 °C	1h	3/1	834,13
AC60021	600 °C	2h	1/1	687,06
AC60022	600 °C	2h	2/1	837,90
AC60023	600 °C	2h	3/1	835,50
AC60031	600 °C	3h	1/1	1275
AC60032	600 °C	3h	2/1	1244.09
AC60033	600 °C	3h	3/1	970,02

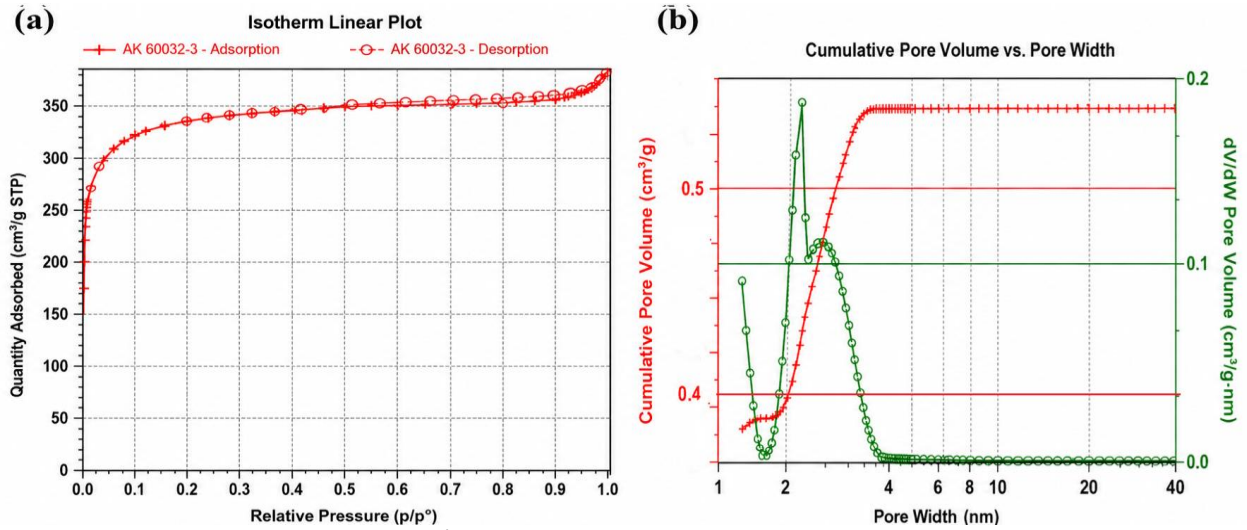


Figure 6. (a)N2 adsorption/desorption isotherms and (b)pore size distributions of AC60032

Table 3. Porosity and surface area metrics of AC60032

Sample	S_{BET}, m^2/g	S_{micro} m^2/g	V_{total}, cm^3/g	V_{micro} cm^3/g	V_{meso} cm^3/g	D_P
AC60032	1244.09	1082.9	0.5449	0.36995	0.17497	2.8146

Table 4. Elemental analysis of AC60032 and PP

Sample	C%	H%	N%	S%	O%
PP	43,61	5,74	0,16	0,00	50,49
AC60032	72,73	1,74	0,12	0,00	25,41

Table 5. PP and AC60032 Proximate Analysis

Material	Solid Matter (wt, %)	Moisture (wt, %)	Volatile (wt, %)	Ash wt, %	Fixed Carbon (wt, %)
PP	93,971	6,029	76,645	3,209	14,117
AC60032	82,693	17,307	14,05	0,660	67,983

The pore structure characteristics of AC60032 were further evaluated by N_2 adsorption-desorption isotherm analysis. As shown in Figure 6(a), a sharp increase in N_2 adsorption at low relative pressure ($p/p_o < 0.1$) was observed, indicating the dominance of microporous structures and a Type I isotherm according to the IUPAC classification (Tian et al. 2020). The absence of a significant hysteresis loop suggests limited mesopore contribution and the presence of narrow micropores (Dragan et *al.* 2021; Lai et *al.* 2020). The pore parameters of AC60032 are presented in Table 3. AC60032 exhibited a total pore volume of 0.5449 cm^3/g and a micropore volume of 0.36995 cm^3/g, indicating a predominantly microporous structure. The pore size distribution in Figure 6(b) shows that most pores are below 5 nm. According to IUPAC classification, pores are categorized as micropores (<20 Å), mesopores (20–500 Å), and macropores (>500 Å) (Joseph, 2021). The developed porous structure provides favourable characteristics for dye adsorption.

3.6. Elemental analysis and proximate analysis

The data from the proximate and elemental analysis of ground pineapple peel and AC60032 are given in table 4 and table 5. The elemental analysis results show that 43.61% of the PP consists of C. Its high carbon content shows that it is suitable for manufacturing activated carbon (Allende et *al.* 2023). The C content of AC60032 appears to increase to 72.73%. The elemental analysis results showed that the carbon content increased from 43.61% in PP to 72.73% in AC60032 after K_2CO_3-assisted activation, indicating the formation of a more carbon-rich structure. The oxygen content was calculated by difference using the equation: O (%) = 100 − (C + H + N + S + Ash). Although the increased carbon content indicates successful carbonization, the high surface area and adsorption capacity of AC60032 cannot be attributed solely to carbon content, as they are also influenced by pore development, activation conditions, and surface chemistry. The proximate analysis showed that the fixed carbon content increased from 14.12% in PP to 67.98% in AC60032, confirming the effectiveness of the activation process. The higher moisture content of AC60032 (17.31%) compared with PP (6.03%) may be related to its developed porous structure and oxygen-containing surface functional groups, which enhance moisture adsorption and hydrophilic characteristics (Marsh and Rodríguez-Reinoso 2006, Ioannidou and Zabaniotou

2007). The low ash content of AC60032 (0.66%) indicates the effective removal of inorganic residues during the washing process.

3.7. Effect of initial solution pH on Yellow RR adsorption

The adsorption behaviour of Yellow RR was investigated by varying the initial pH of 100 mL dye solutions (100 mg/L) between pH 2–6. The stirring speed, adsorbent dosage, particle size, temperature, and contact time were kept constant at 200 rpm, 0.1 g, 0–109 µm, 293 K, and 240 min, respectively. The pH adjustment was performed using H_2SO_4 and NaOH solutions. As shown in Figure 7(a), increasing the initial pH resulted in a decrease in the adsorption capacity of Yellow RR, with the highest adsorption capacity obtained at pH 2 (74.34 mg/g). Similar behavior has been reported for anionic dyes, where acidic conditions can enhance adsorption performance (Vojnović et al. 2022). The adsorption capacity decreased to 57.95 mg/g at pH 4 and further declined to 47.95 mg/g at pH 6. This reduction may be attributed to changes in the surface charge of AC60032 and the ionization state of Yellow RR molecules at different pH conditions. At higher pH values, the negatively charged surface of AC60032 may increase electrostatic repulsion with the anionic dye molecules, leading to reduced adsorption. In addition, interactions involving surface functional groups, hydrogen bonding, and π–π interactions between the dye molecules and the carbon structure may also contribute to the adsorption process (Pimentel et al. 2025).

3.8. Effect of adsorbent dosage on Yellow RR adsorption

To evaluate the effect of adsorbent dosage, 0.1, 0.2, 0.3, and 0.4 g of AC60032 were added to 100 mL of Yellow RR solutions with initial dye concentrations of 20-120 mg L^{-1}, and the adsorption performance was investigated. The pH, stirring speed, particle size, temperature, and contact time were kept constant at 2, 200 rpm, 0–109 µm, 293 K, and 240 min, respectively.

As shown in Figure 7(b), the adsorption capacity decreased as the AC60032 dosage increased from 0.1 to 0.4 g. This reduction may result from the increased number of available adsorption sites relative to the fixed amount of dye, leaving a greater proportion of sites unsaturated and reducing the amount of dye adsorbed per unit mass of adsorbent (Strebel et al., 2024). The highest adsorption capacity was therefore obtained at an AC60032 dosage of 0.1 g.

3.9. Effect of contact time on Yellow RR adsorption

The effect of contact time on the adsorption capacity of Yellow RR was investigated using dye solutions with initial concentrations of 20-120 mg/L over a contact time range of 60-240 min. Different initial dye concentrations were selected to evaluate the effect of concentration on adsorption kinetics and to determine the adsorption behaviour of Yellow RR under different pollutant loading conditions. The pH, stirring speed, adsorbent dosage, particle size, and temperature were kept constant at 2, 200 rpm, 0.1 g, 0–109 µm, and 293 K, respectively. As shown in Figure 7(c), a sharp increase in adsorption capacity was observed during the first 60 min for all dye concentrations, indicating the rapid occupation of the available active sites on the AC60032 surface. Thereafter, the adsorption capacity gradually decreased, and equilibrium was reached between 120 and 180 min. At 240 min, the adsorption capacity remained almost constant. The highest adsorption capacity (81.47 mg/g) was obtained at an initial dye concentration of 120 mg/L, while lower capacities were observed at lower initial concentrations. Similar adsorption behaviour, characterized by a rapid initial adsorption stage followed by a slower approach to equilibrium, has also been reported in previous studies (Bakhsh et al. 2022; Jabar et al. 2020; Pieczykolan 2025).

3.10. Effect of stirring speed on Yellow RR adsorption

The effect of stirring speed on the adsorption capacity of Yellow RR was investigated at stirring speeds ranging from 100 to 250 rpm using a 100 mg/L dye solution. Adsorption capacity was monitored over a contact time of 240 min, while the adsorbent dosage, temperature, and pH were kept constant at 0.1 g, 293 K, and pH 2, respectively. Figure 7(d), illustrates that increasing stirring speed led to higher adsorption capacity. While the lowest adsorption capacity was observed at 100 rpm (69.18 mg/g), mass transfer accelerated at 250 rpm and the highest adsorption capacity was reached (81.97 mg/g). The increase in stirring speed reduced the interfacial diffusion resistance in the boundary layer, facilitating dye removal and improving efficiency (de Farias Silva et *al*. 2020).

3.11. Effect of solution concentration on Yellow RR adsorption

The effect of initial Yellow RR concentration on the adsorption capacity was investigated by monitoring the adsorption process at specific time intervals until equilibrium was reached. The stirring speed, adsorbent dosage, pH, particle size, and temperature were kept constant at 200 rpm, 0.1 g, 0–109 µm, pH 2, and 293 K, respectively. With increasing Yellow RR concentration, the adsorption capacity (q_e) increased due to the higher availability of dye molecules in the solution and the enhanced driving force for mass transfer (Al-Saeedi et al.

2023). As shown in Figure 7(e), the adsorption capacity increased from 19.18 mg/g at 20 mg/L to 81.47 mg/g at 120 mg/L using 0.1 g of adsorbent. This behaviour can be attributed to the increased concentration gradient between the dye solution and the AC60032 surface, which promotes the transfer of dye molecules to the available adsorption sites. At lower initial dye concentrations, fewer dye molecules are available for interaction with the adsorbent surface, resulting in lower adsorption capacity (Sadoun et al. 2023; Aseeri et al. 2025).

3.12. Effect of temperature on Yellow RR adsorption

Temperature effect on adsorption capacity of Yellow RR by AC60032 were examined at 293, 298, 303, 308, 313, and 323 K. The adsorption process was performed using 20-100 mg/L dye solutions, 0.1 g of AC60032 (particle size 0-109 µm), with 200 rpm mixing rate at pH 2, for 240 minutes. As shown in Figure 7(f), the adsorption capacity of Yellow RR increased with increasing temperature, particularly at higher initial dye concentrations. The adsorption capacity increased from lower values at 293 K to higher values at 323 K, indicating that temperature positively influenced the adsorption process. This behaviour may be associated with enhanced mobility of dye molecules and improved interaction between Yellow RR molecules and the AC60032 surface at elevated temperatures. Similar temperature-dependent increases in adsorption capacity have been reported for dye adsorption systems (Gonçalves et al. 2022; Saleem et al. 2024).

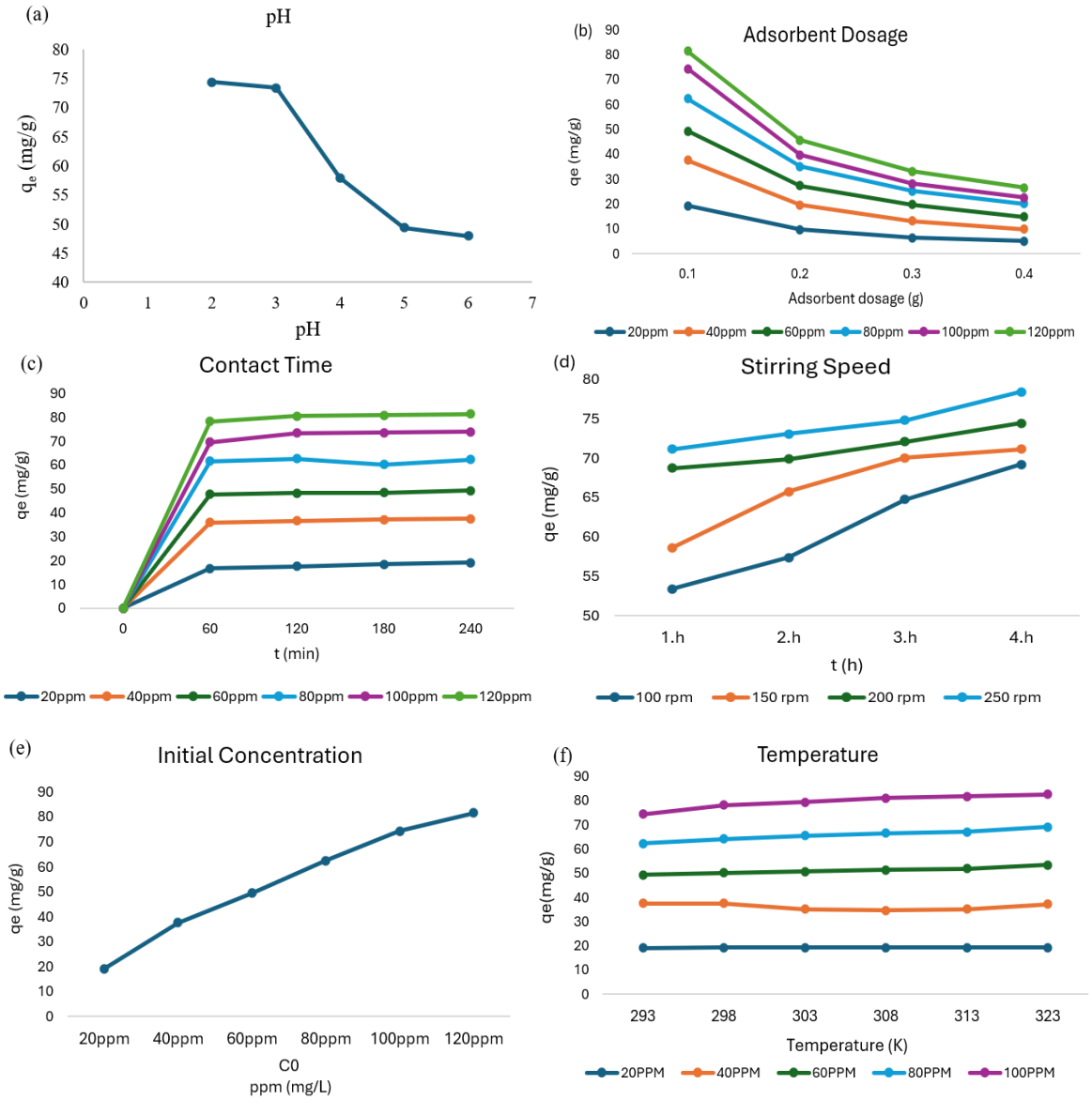


Figure 7. Parameters affecting adsorption of Yellow RR(a) pH, (b) Adsorbent Dosage, (c) Contact Time, (d) Stirring Speed, (e) Initial Concentration, (f) Effect of Temperature on Adsorption

3.13. Adsorption isotherms

Figure 8 illustrates the adsorption isotherms of Yellow RR on AC60032 at 293 K, fitted using (a) Langmuir, (b) Freundlich, (c) Temkin, and (d) Dubinin–Radushkevich (D–R) models.

For the isotherm analysis, the initial Yellow RR concentration was varied from 20 to 100 mg/L while maintaining constant experimental conditions: pH 2, adsorbent dosage of 0.1 g, contact time of 240 min, particle size of 0–109 µm, and stirring speed of 200 rpm. The isotherm constants obtained at 293–323 K are presented in Table 6. Although the Langmuir model appeared suitable at 293 K, analysis of the data in Table 5 within the 293 -323 K range revealed that the Freundlich model fits better overall. The highest R^2 value for Langmuir was observed at 293 K, but at higher temperatures this trend was not maintained, indicating that Freundlich provides a more consistent description of the adsorption behavior. Similar equilibrium behavior has been reported for reactive dye adsorption onto AC60032, where the Freundlich model provided a better fit for heterogeneous adsorption systems (Sahu et *al.* 2020; Kouhail et *al.* 2020)

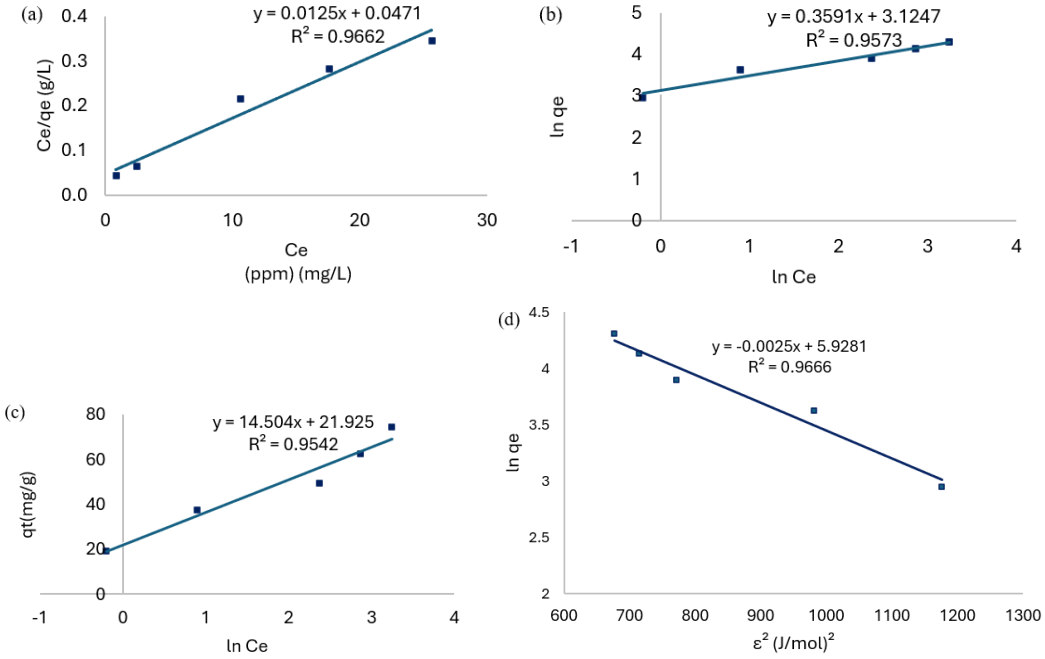


Figure 8. (a) Langmuir, (b)Freundlich, (c)Temkin, (d)Dubinin-Radushkevich (D-R) isotherms for Yellow RR adsorption on AC60032 at 293K

Table 6. Calculated isotherm constants for AC60032-Yellow RR interaction (Langmuir, Freundlich, Dubinin–Radushkevich, Temkin)

YRR Isotherms							
	T(K)	293	298	303	308	313	323
Langmuir	q_{max} (mg/g)	80	84.7458	96.15385	103.093	103.093	105.02
	K_L (L/mg)	0.2654	0.2565	0.1612	0.1443	0.1527	0.1002
	R_L (100mg/L– 20mg/L)	0.00012-0.00060	0.00011-0.00056	0.00007-0.00036	0.00008-0.00042	0.00009-0.00043	0.000010-0.00049
	R^2	0.9662	0.951	0.9454	0.9366	0.9291	0.8204
Freundlich	n	2.7847	2.5947	2.3685	2.2810	2.2366	2.1537
	K_F	22.7530	22.8031	20.5425	20.3646	20.5364	22.4188
	R^2	0.9573	0.9666	0.9753	0.9558	0.966	0.9991
D-R	q_{max} (mg/g)	375	450	449	451	441	510
	K	0.0025	0.0026	0.0026	0.0025	0.0024	0.0023
	E (kJ/mol)	14.02	13.83	13.62	13.56	13.64	13.27
	R^2	0.94	0.96	0.96	0.97	0.97	0.98
Temkin	B_T (J/mol)	1.7445	1.9126	2.0500	2.1675	2.2030	2.3873
	K_T	4.5342	3.9748	2.9771	2.8025	2.7502	2.8951
	R^2	0.9542	0.9406	0.7832	0.851	0.8665	0.9642

The adsorption isotherm parameters presented in Table 6 indicate that the Freundlich model provided the best fit for Yellow RR adsorption onto AC60032, with R^2 values ranging from 0.9573 to 0.9991. The high correlation coefficients suggest that adsorption occurs on a heterogeneous surface with possible multilayer

adsorption characteristics (Shikuku et al. 2021; Ajala et al. 2023). The adsorption behavior followed the order of Freundlich > Dubinin–Radushkevich (D–R) > Langmuir > Temkin based on the obtained R^2 values. The Freundlich constant (n) values ranged between 2.15 and 2.78, all greater than 1, confirming the favorable adsorption of Yellow RR onto AC60032 (Bazan-Wozniak and Pietrzak 2023; Güneş 2023; Alamzeb *et al.* 2022).

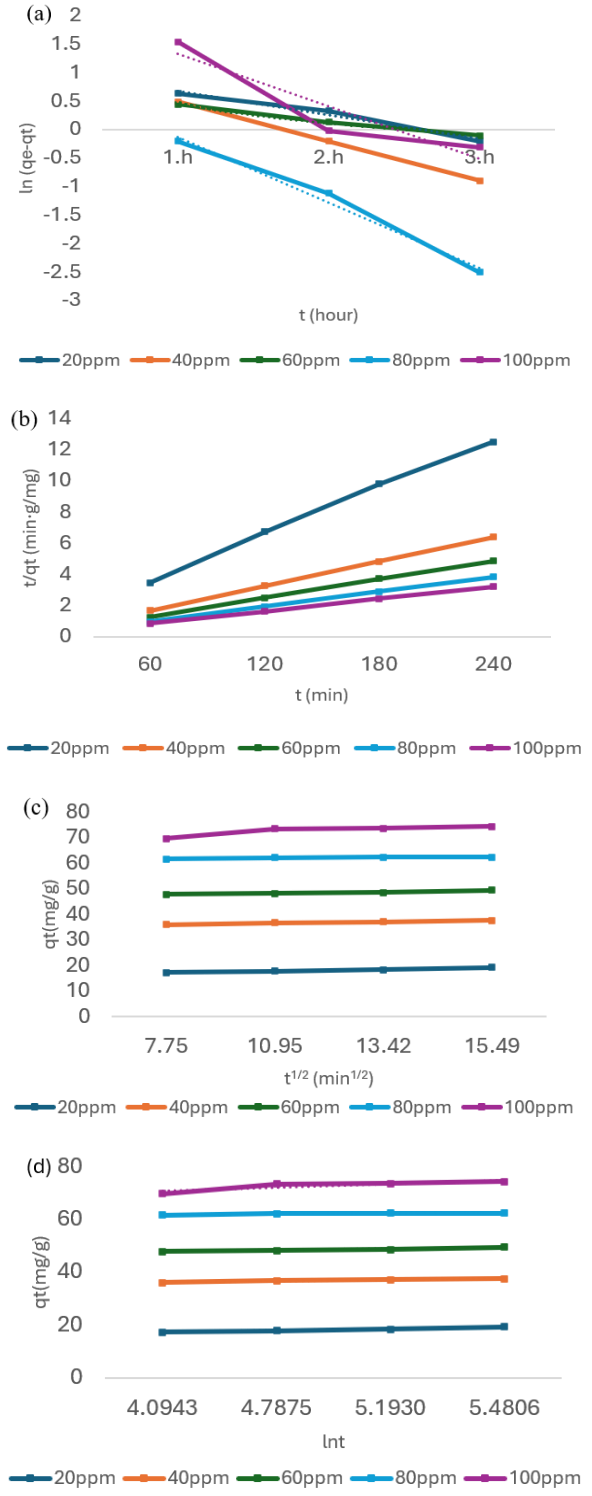


Figure 9. (a) Pseudo first order, (b) Pseudo second order, (c) Intraparticle diffusion, (d) Elovich kinetics models for the adsorption of Yellow RR on AC60032 at 293K.

The D–R model also showed good agreement with the experimental data (R^2 = 0.94–0.98). The calculated adsorption energy values (E = 13.27–14.02 kJ/mol) indicate that the adsorption process is mainly governed by physical interactions. Although the Langmuir model showed lower correlation coefficients, the increased q_{max} values, confirming the enhanced adsorption capacity at higher temperatures. This trend is consistent with the positive ΔH° value obtained from thermodynamic analysis, indicating the endothermic nature of Yellow RR adsorption. According to Le Chatelier's principle, an increase in temperature shifts the equilibrium towards the endothermic direction, resulting in enhanced adsorption capacity under higher temperature conditions (Olivito et al. 2022). The R_L values between 0 and 1 at all temperatures confirmed the favorable adsorption process under the studied conditions (Obulapuram et *al.* 2021; Khapre et *al.* 2022). Furthermore, the decrease in RL values with increasing initial dye concentration from 20 to 100 mg/L indicates that the adsorption process becomes more favorable at higher dye concentrations (Zhang, 2023; Tichem et *al.* 2023). The Temkin model showed moderate agreement with the experimental data, with R^2 values ranging from 0.7832 to 0.9642. The calculated B_t values increased from 1.7445 to 2.3873 J/mol with increasing temperature, suggesting a gradual change in adsorption energy due to adsorbate-adsorbent interactions. Lower R^2 values at intermediate temperatures indicate that these interactions may not be the dominant factor governing the adsorption process.

3.14. Adsorption Kinetics

Figure 9 shows the kinetic models applied to Yellow RR adsorption on AC60032 at 293 K, including (a) pseudo-first-order, (b) pseudo-second-order, (c) intraparticle diffusion, and (d) Elovich models.

The correlation between adsorption capacity and contact time was scrutinized at six distinct temperatures (Purnomo et *al.* 2023, Chouchane et *al.* 2023). Pseudo first-order, Pseudo second-order, intraparticle diffusion and Elovich models were used to interpret the adsorption kinetics and presented in Table 7. The positive intercept values (C) obtained from the intraparticle diffusion plots indicate the presence of boundary layer effects, suggesting that intraparticle diffusion was not the sole controlling step during adsorption (Weber and Morris 1963, Kannan and Sundaram 2001, Wu et *al.* 2009).

Table 7. Calculated kinetics constants for AC60032-Yellow RR interaction (Pseudo first order, pseudo second order, intraparticle diffusion, Elovich kinetics)

			Pseudo 1st order			Pseudo 2nd order			
T (K)	C_0 (mgL^{-1})	q_e (exp) (mgg^{-1})	q_e (calc) (mgg^{-1})	k_1 (min^{-1})	R^2	q_e(calc) (mgg^{-1})	k_2(gmg^{-1} min^{-1})	H(mgg^{-1} min^{-1})	R^2
293K	20	19.1803	2.9701	0.4165	0.9756	19.8807	0.0046	1.8272	0.9982
	40	37.541	3.2785	0.6931	1	38.1679	0.0066	9.5711	0.9999
	60	49.3443	2.0251	0.2733	0.9954	49.7512	0.0062	15.4025	0.9997
	80	62.377	2.8033	1.1513	0.9863	62.5	0.0143	55.7748	1
	100	74.3443	9.5143	0.9229	0.8636	75.7576	0.0027	15.7331	0.9999
298K	20	19.2213	2.3912	0.3345	0.9911	19.802	0.0052	2.0332	0.9981
	40	37.541	3.2785	0.6931	1	38.1679	0.0066	9.5711	0.9999
	60	50.1639	2.0214	0.8047	0.9574	50.5051	0.0132	33.7882	1
	80	64.1803	3.6477	0.5493	0.9559	64.9351	0.0051	21.3262	0.9999
	100	78.1967	2.4066	0.6609	0.9992	78.7402	0.0091	56.3304	1
303K	20	19.2623	8.7094	0.7438	0.9763	21.645	0.0022	1.0216	0.9983
	40	36.4754	4.9249	0.1003	0.9593	37.7358	0.0017	2.4776	0.9879
	60	50.7377	1.3477	0.602	0.9167	51.0204	0.0129	33.7058	1
	80	65.5738	5.5924	0.7107	0.8892	66.6667	0.0388	172.2685	0.9999
	100	79.4262	1.4016	0.4581	0.9194	80	0.0132	84.5417	1
308K	20	19.2623	3.769	0.4975	0.75	20.2429	0.0053	2.1655	0.9982
	40	36.3115	3.7882	0.1897	0.997	37.1747	0.0027	3.7167	0.9964
	60	51.3934	1.6392	0.4778	0.9717	51.8135	0.0105	28.2337	1
	80	66.6393	7.0259	0.752	0.9339	67.5676	0.0031	14.2785	0.999
	100	81.0656	3.3781	1.1513	0.863	81.3008	0.0127	83.8177	1
313K	20	19.2623	2.3289	0.317	0.882	19.9203	0.008	3.183	0.9992
	40	36.0656	2.4628	0.2482	0.9315	36.63	0.0046	6.1402	0.999
	60	51.8033	1.9024	0.8047	0.9936	52.0833	0.0124	33.6947	1
	80	67.0492	1.653	0.752	0.9843	67.1141	0.0124	55.6632	1
	100	81.7213	3.6241	0.973	0.9096	81.9672	0.0083	55.8904	1
323K	20	19.2623	11.1462	0.9041	0.75	19.305	0.1123	41.8517	1
	40	36.0656	4.002	0.901	0.8	36.1011	0.0183	23.8564	0.9995
	60	53.0082	2.0232	0.1711	0.9976	53.4759	0.0049	14.1351	0.9995
	80	70.0246	1.9054	0.241	0.9998	70.4225	0.0057	28.0944	0.9998
	100	86.6393	6.0321	0.1097	0.9998	87.7193	0.0015	11.3898	0.9974

		Elovich			Intraparticle Diffusion		
T (K)	C_0 (mgL^{-1})	β(gmg^{-1})	α ($mg(gmin)^{-1}$)	R^2	k_{-id}(mgg^{-1} $min^{1/2}$)	C(mgg^{-1})	R^2
293	20	1.6051	2.32E+11	0.9857	0.623	16.598	0.9857
	40	1.8769	4.54E+28	0.9657	0.5328	35.492	0.9657
	60	2.0333	2.42E+41	0.9278	0.4918	47.213	0.9278
	80	3.6969	1.00E+98	0.8963	0.2705	61.393	0.8963
	100	0.7012	1.66E+21	0.7751	1.4262	69.18	0.7751
298	20	1.8345	1.61E+13	0.9606	0.5451	16.906	0.9606
	40	1.8769	4.54E+28	0.9657	0.5328	35.492	0.9657
	60	3.5881	8.99E+75	0.9797	0.2787	49.098	0.9797
	80	1.5063	1.16E+40	0.9979	0.6639	61.516	0.9979
	100	2.49	3.03E+82	0.978	0.4016	76.639	0.978
303	20	0.6667	1.67E+04	0.8584	1.5	13.975	0.8584
	40	0.7262	3.99E+09	0.7514	1.377	30	0.7514
	60	3.9355	2.77E+84	0.9109	0.2541	49.754	0.9109
	80	1.196	1.91E+32	0.976	0.8361	62.295	0.976
	100	3.5881	2.70E+121	0.9797	0.02787	78.279	0.9797
308	20	1.2323	5.89E+08	0.6	0.8115	16.557	0.6
	40	1.0167	1.18E+14	0.8571	0.9836	31.885	0.8571
	60	2.9753	1.54E+64	0.9689	0.3361	50.041	0.9689
	80	0.9839	6.31E+26	0.9856	1.0164	62.705	0.9856
	100	1.2708	1.08E+09	0.6	0.2951	79.959	0.9391

Table 7. (continued) Calculated kinetics constants for AC60032-Yellow RR interaction (Pseudo first order, pseudo second order, intraparticle diffusion, Elovich kinetics)

		Elovich			Intraparticle Diffusion		
T (K)	C_0 (mgL^{-1})	β(gmg^{-1})	α (mg(gmin)$^{-1}$)	R^2	k_{-id}(mgg^{-1} min$^{1/2}$)	C(mgg^{-1})	R^2
313	20	1.8484	4.82E+13	0.6	0.5656	17.377	0.6
	40	1.6485	4.98E+23	0.9066	0.6066	33.402	0.9066
	60	3.6969	9.10E+80	0.9595	0.2705	50.779	0.9595
	80	4.0667	1.40E+116	0.9783	0.2459	66.107	0.9783
	100	2.49	2.18E+86	0.9623	0.4016	80.205	0.9623
323	20	20.3252	1.90E+167	0.6	0.0492	19.098	0.6
	40	10.989	1.40E+174	0.0986	0.091	36.709	0.0986
	60	1.8741	7.92E+40	0.8377	0.5336	50.586	0.8377
	80	2.107	7.01E+61	0.9047	0.4746	67.939	0.9047
	100	0.5981	4.93E+20	0.7636	1.6721	78.811	0.7636

The adsorption of Yellow RR with AC60032 was studied between 20-100 mg/L at 293-323K with other parameters remaining constant (pH 2, stirring speed 200 rpm, particle size 0-109 µm, adsorbent dose 0.1 g, contact time 240 min). The suitability of kinetic models was evaluated not only by R^2 values but also by the agreement between experimental and calculated q_e values. Although the pseudo-first-order model showed high R^2 values under some conditions, the pseudo-second-order model provided closer q_e,cal values and better described the adsorption kinetics of Yellow RR onto AC60032 (Kızıl et al., 2024; Sahu et al., 2020). The initial adsorption capacity H (mg·g^{-1}·min^{-1}) generally increased with temperature. This confirms that the reaction proceeds endothermically (Huang, Y. T. and Shih 2025, Al-Harby et *al.* 2021). The linear plots for the intraparticle diffusion region do not intersect the origin, showing that both intraparticle diffusion and boundary layer diffusion may contribute to the adsorption process (Pan et *al.* 2020, Zaidi et *al.* 2021).

Increasing the initial Yellow RR concentration resulted in higher intercept values (I) in the intraparticle diffusion model, suggesting a greater contribution from boundary-layer effects to the adsorption process. The Elovich parameter α varied with both temperature and initial dye concentration, showing no consistent trend (Pan et *al*. 2020, Jameer et *al.* 2017). The calculated α values from the Elovich model showed very high magnitudes under some conditions. Since α is an empirical parameter obtained from the intercept of the linearized Elovich equation, it is sensitive to mathematical fitting and should be interpreted with caution. Similar observations have been reported in the literature, indicating that the Elovich parameters obtained from linearized equations may show unrealistic magnitudes due to mathematical fitting limitations and should be interpreted as empirical parameters rather than absolute physical constants (Ho and McKay, 2003; Wu et al., 2009). The experimental equilibrium adsorption capacities (q_e,exp) at 20, 40, and 60 mg/L were relatively similar at different temperatures, indicating that sufficient active sites were available on AC60032 within this concentration range. Therefore, temperature had a limited effect on adsorption capacity under these conditions. At higher dye concentrations, the increased concentration gradient enhanced mass transfer between the solution and adsorbent surface, leading to more noticeable changes in q_e,exp values. The adsorption capacity is influenced by the surface characteristics, availability of active sites, and adsorbate–adsorbent interactions (Kyzas and Kostoglou, 2014).

3.15. Adsorption thermodynamics

Figure 10 illustrates the thermodynamic analysis of Yellow RR adsorption, while Table 8 presents the corresponding thermodynamic constants.

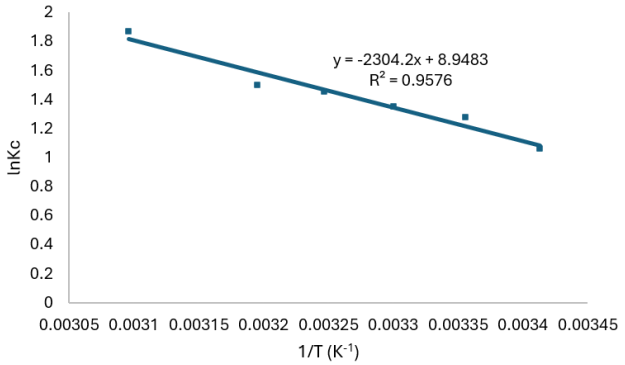


Figure 10. Van't Hoff plot of lnK_c vs 1/T for Yellow RR adsorption

Table 8. Calc. thermodynamic constants of Yellow RR adsorption

T (K)	Kc (L/mg)	ΔH (kJ/mol)	ΔG (kJ/mol)	ΔS (kJ/mol K)
293	2.89776	19.1571	-2.640957	0.0743
298	3.58646		-3.012938	
303	3.86055		-3.384919	
308	4.28138		-3.756900	
313	4.47085		-4.128881	
323	6.48466		-4.872842	

The Gibbs free energy was calculated using the following equation:

$$K_c = q_e/C_e \quad (3)$$

Substituting the equilibrium constant (K) into Equation 2 gives the standard Gibbs free energy of adsorption.

$$\Delta G^\circ = -RT\ln K \quad (4)$$

In accordance with the Van't Hoff equation:

$$\ln K = -\Delta G^\circ \frac{1}{R} * \frac{1}{T} = -\frac{\Delta H^\circ}{R} * \frac{1}{T} + \frac{\Delta S^\circ}{R} \quad (5)$$

(Rahman et *al.* 2021, Asadullah et *al.* 2022)

R: Gas constant (8,314 J/molK)

Based on these equations, a mathematical relationship between K and 1/T can be derived. Derivation of the Van't Hoff equation enables the calculation of thermodynamic parameters through plotting $\ln K_c$ against 1/T. The slope of the Van't Hoff plot corresponds to −ΔH°/R enthalpy, whereas the intercept reveals the change in entropy (ΔS°), thereby offering insights into the characteristics of the adsorption process (Li et *al.* 2023, Mahmood et *al*. 2024).

In the adsorption experiment of Yellow RR with AC60032, other variables, including pH (2), adsorbent dose (0.1 g), contact time (240 min), particle size (0–109 µm), and stirring speed (200 rpm), were kept constant, while the temperature range was maintained between 293-323 K.

The thermodynamic parameters describe Yellow RR interactions with AC60032 adsorption sites during adsorption and should be interpreted separately from preparation parameters that determine its pore structure and surface properties.

The negative ΔG° values obtained at 293–323 K confirm the natural spontaneity of Yellow RR adsorption onto AC60032 Luo et *al.* 2020). With rising temperature, these values decrease, leading to better adsorption at higher temperatures (Sirach and Dave 2023, Girish 2025).

The positive ΔH° value (19.15 kJ/mol) confirms the endothermic nature of Yellow RR adsorption onto AC60032. The obtained ΔH° value reflects the energy requirement of dye–adsorbent interactions and does not indicate a direct relationship with the activation temperature or surface area of the prepared AC60032 According to the reported classification, enthalpy values between 2.1 and 20.9 kJ/mol are associated with physical adsorption, whereas higher values are related to chemisorption (Tran 2022, Girish 2025). Therefore, the ΔH° value obtained in this study suggests that Yellow RR adsorption onto AC60032 is governed by physical interactions (Ullah et al. 2024).

The positive ΔS° value indicates an increase in randomness at the solid–solution interface during adsorption, which may be attributed to the release of water molecules surrounding the dye molecules during adsorption (Sahmoune 2019).

4. Conclusion

This study presents a sustainable waste-to-value approach for the conversion of pineapple peel, an abundant agricultural residue, into a highly efficient activated carbon adsorbent through K_2CO_3-assisted chemical activation. The optimized AC60032 sample achieved a high BET surface area of 1244.09 m^2/g with a micropore-dominated structure, demonstrating the effectiveness of the selected activation strategy in developing adsorption-active carbon frameworks.

The developed AC60032 exhibited excellent capability for Reactive Yellow RR removal, reaching a maximum adsorption capacity of 105.02 mg/g at 323 K. The Freundlich model provided the best fit to the equilibrium data (R^2 up to 0.9991), indicating a heterogeneous adsorption surface, while the pseudo-second-order model adequately described the adsorption kinetics. The combined characterization and modelling results suggest that Yellow RR adsorption was influenced by the developed porous structure, surface functional groups, and dye-carbon interactions.

Thermodynamic evaluation demonstrated that Yellow RR adsorption onto AC60032 was spontaneous (negative ΔG° values) and endothermic (ΔH° = +19.15 kJ/mol), with adsorption mainly governed by physical interactions. These findings confirm that the produced carbon possesses favourable regeneration potential compared with conventional single-use treatment materials.

The main scientific contribution of this study is the demonstration that K_2CO_3 activation of pineapple peel can provide a highly porous and effective carbon material for reactive dye removal, offering an alternative sustainable route to commonly investigated activation strategies. Beyond adsorption performance, this research highlights the transformation of agricultural waste into a value-added functional material, contributing to circular economy principles and sustainable wastewater treatment. Therefore, pineapple peel-derived AC60032 represents a promising candidate for future application in textile wastewater remediation.

Declaration of Ethical Standards

This study was prepared based on the doctoral dissertation entitled "Investigation of the Kinetic, Isotherm, and Thermodynamic Behavior of Reactive Yellow RR Dye Adsorption Using Activated Carbon Produced from Pineapple Peel", completed under the supervision of Prof. Dr. Unsal Acikel.

It is hereby declared that scientific and ethical principles were followed throughout the preparation of this study, and that all sources and references utilized have been properly cited in the bibliography.
The authors declare that they comply with all ethical standards.

Credit Authorship Contribution Statement

Author 1: Conceptualization, Methodology / Study Design, Investigation, Resources, Validation, Formal Analysis, Data Curation, Writing – Original Draft, Writing – Review and Editing, Visualization, Project Administration.
Author 2: Supervision, Funding Acquisition.
Author 3: Investigation.
Author 4: Writing – Review and Editing, methodology and software, Resources, Visualization.

Declaration of Competing Interest

The authors have no conflicts of interest to declare regarding the content of this article.

Data Availability Statement

All data generated or analyzed during this study are included in this published article.

Acknowledgement

This work was supported by the Sivas Cumhuriyet Universitesi - Bilimsel Arastirma Projeleri Koordinasyon Birimi [Project Number: M-2024-866].

5. References

Ajala, O.A., Akinnawo, S.O., Bamisaye, A., Adedipe, D.T., Adesina, M.O., Okon-Akan, O.A., et al., 2023. Adsorptive removal of antibiotic pollutants from wastewater using biomass/biochar-based adsorbents. *RSC Advances*, 13, **7**, 4678–4698. https://doi.org/10.1039/D2RA06436G

Alamzeb, M., Khan, R. and Shah, S.A., 2022. Kinetic, thermodynamic and adsorption isotherm studies of detoxification of Eriochrome Black T dye from wastewater by native and washed garlic peel. *Water*, 14, **22**, 3713. https://doi.org/10.3390/w14223713

Al-Harby, N.F., Albahly, E.F. and Mohamed, N.A., 2021. Kinetics, isotherm and thermodynamic studies for efficient adsorption of Congo Red dye from aqueous solution onto novel cyanoguanidine-modified chitosan adsorbent. *Polymers*, 13, **24**, 4446. https://doi.org/10.3390/polym13244446

Allende, S., Liu, Y., Zafar, M.A. and Jacob, M.V., 2023. Nitrite sensor using activated biochar synthesised by microwave-assisted pyrolysis. *Waste Disposal & Sustainable Energy*, 5, **1**, 1–11. https://doi.org/10.1007/s42768-022-00120-4

Al-Saeedi, S.I., Ashour, M. and Alprol, A.E., 2023. Adsorption of toxic dye using red seaweeds from synthetic aqueous solution and its application to industrial wastewater effluents. *Frontiers in Marine Science*, 10, 1202362. https://doi.org/10.3389/fmars.2023.1202362

Anusonthiwong, T., Suwatanapongched, N., Surawattanawiset, J., Chittreisin, N., Ittisanronnachai, S., Sangtawesin, T. and Anantachaisilp, S., 2025. Activated carbon derived from rice husks enhanced by methylene blue and gamma irradiation for supercapacitor applications. *RSC Sustainability*, 3, **3**, 1507–1515. https://doi.org/10.1039/D4SU00701H

Aragaw, T.A. and Bogale, F.M., 2021. Biomass-based adsorbents for removal of dyes from wastewater: a review. Frontiers in Environmental Science, 9, 764958. https://doi.org/10.3389/fenvs.2021.764958

Asadullah, M., Ain, Q. and Ahmad, F., 2022. Investigation of a low cost, stable and efficient adsorbent for the fast uptake of Cd (II) from aqueous media. *Advanced Journal of Chemistry, Section A*, 5, **4**, 345–356.

Aseeri, A.A., Faez Sead, F., Altalbawy, F., Yousif, N., Salih Sahib, A., Saad Abdulali, Z., et al., 2025. Design of a scandium-integrated MOF hybrid hydrogel for simultaneous dye adsorption and antibacterial activity. Frontiers in Chemistry, 13, 1659983. https://doi.org/10.3389/fchem.2025.1659983

Bakhsh, E.M., Bilal, M., Ali, M., Ali, J., Wahab, A., Akhtar, K., Fagieh, T.M., Danish, E.Y., Asiri, A.M. and Khan, S.B., 2022. Synthesis of activated carbon from Trachycarpus fortunei seeds for the removal of cationic and anionic dyes. Materials, 15, **6**, 1986. https://doi.org/10.3390/ma15061986

Bazan-Wozniak, A. and Pietrzak, R., 2023. Adsorption of cationic dye on nanostructured biocarbons: Kinetic and thermodynamic study. *Applied Nanoscience*, 13, **10**, 6787–6801. https://doi.org/10.1007/s13204-023-02775-9

Chouchane, T., Boukari, A., Khireddine, O., Chibani, S. and Chouchane, S., 2023. Equilibrium, kinetics, and thermodynamics of batch adsorption of Mn (II) ions on blast furnace slag (BFS) and kaolin (KGA). Journal of Engineering and Applied Science, 70, **1**, 58. https://doi.org/10.1186/s44147-023-00218-4

de Farias Silva, C.E., da Gama, B.M.V., da Silva Gonçalves, A.H., Medeiros, J.A. and de Souza Abud, A.K., 2020. Basic-dye adsorption in albedo residue: Effect of pH, contact time, temperature, dye concentration, biomass dosage, rotation and ionic strength. Journal of King Saud University - Engineering Sciences, 32, **6**, 351–359. https://doi.org/10.1016/j.jksues.2019.04.006

Dragan, G., Kutarov, V., Schieferstein, E. and Iorgov, A., 2021. Adsorption hysteresis in open slit-like micropores. *Molecules*, 26, **16**, 5074. https://doi.org/10.3390/molecules26165074

Duraisamy, N., Shenniangirivalasu Kandasamy, K., Dhandapani, E., Kandiah, K., Panchu, S.J. and Swart, H.C., 2025. Biomass derived 3D hierarchical porous

activated carbon for solid-state symmetric supercapacitors. Journal of Inorganic and Organometallic Polymers and Materials, 1–23. https://doi.org/10.1007/s10904-025-03837-x

Dutta, S., Gupta, B., Srivastava, S.K. and Gupta, A.K., 2021. Recent advances on the removal of dyes from wastewater using various adsorbents: A critical review. *Materials Advances*, 2, **14**, 4497–4531. https://doi.org/10.1039/D1MA00354B

El-Sayed, S.A., Khass, T.M. and Mostafa, M.E., 2024. Thermal degradation behaviour and chemical kinetic characteristics of biomass pyrolysis using TG/DTG/DTA techniques. Biomass Conversion and Biorefinery, **14**, 15, 17779–17803. https://doi.org/10.1007/s13399-023-03926-2

Foo, K.Y., Hameed, B.H., 2012. Porous structure and adsorptive properties of pineapple peel based activated carbons prepared via microwave assisted KOH and K_2CO_3 activation. Microporous and Mesoporous Materials, 148, 1, 191–195. https://doi.org/10.1016/j.micromeso.2011.08.005

Gan, Y.X., 2021. Activated carbon from biomass sustainable sources. *C*, 7, **2**, 39. https://doi.org/10.3390/c7020039

Girish, C.R., 2025. Determination of thermodynamic parameters in adsorption studies: A review. Chemical Papers, 1–20. https://doi.org/10.1007/s11696-025-04218-x

Gonçalves, R.G.L., Lopes, P.A., Pochapski, D.J., de Oliveira, L.C.A., Pinto, F.G., Neto, J.L. and Tronto, J., 2022. Effect of pH, ionic strength, and temperature on the adsorption behavior of Acid Blue 113 onto mesoporous carbon. Environmental Science and Pollution Research, 29, **51**, 77188–77198. https://doi.org/10.1007/s11356-022-21193-y

Ho, Y.S. and McKay, G., 2003. Sorption of dyes and copper ions onto biosorbents. Process Biochemistry, 38, **7**, 1047–1061. https://doi.org/10.1016/S0032-9592(02)00239-X

Hafizah, M.A.E., Manaf, A., Valency, T., Andreas, A. and Manawan, M., 2025. Optimized carbonization and kinetic analysis of palm kernel shell porous carbon for heavy metal adsorption. Indonesian Journal of Chemistry, 25, 3, 787-799. https://doi.org/10.22146/ijc.100714

Ho, Y.S. and McKay, G., 2003. Ho, Y.S. and McKay, G., 2003. Sorption of dyes and copper ions onto biosorbents. Process Biochemistry, 38(7), 1047–1061. https://doi.org/10.1016/S0032-9592(02)00239-X

Huang, Y.T. and Shih, M.C., 2025. Kinetic, isotherm, and thermodynamic modeling of methylene blue adsorption using natural rice husk: A sustainable approach. *Separations*, 12, **8**, 189. https://doi.org/10.3390/separations12080189

Illingworth, J.M., Rand, B. and Williams, P.T., 2022. Understanding the mechanism of two-step, pyrolysis-alkali chemical activation of fibrous biomass for the production of activated carbon fibre matting. Fuel Processing Technology, 235, 107348. https://doi.org/10.1016/j.fuproc.2022.107348

Ioannidou, O., Zabaniotou, A., 2007. Agricultural residues as precursors for activated carbon production—A review. Renewable and Sustainable Energy Reviews, 11, 1966–2005. https://doi.org/10.1016/j.rser.2006.03.013

Jabar, J.M., Odusote, Y.A., Alabi, K.A. and Ahmed, I.B., 2020. Kinetics and mechanisms of Congo Red dye removal from aqueous solution using activated Moringa oleifera seed coat as adsorbent. Applied Water Science, 10, **6**, 1–11. https://doi.org/10.1007/s13201-020-01221-3

Jameer Ahammad, S., Sumithra, S. and Subha, R., 2017. Equilibrium and kinetic studies for the biosorption of Cd (II) in aqueous solution onto almond gum. *International Journal of Chemical Sciences*, 15, **3**, 161.

Jesus, E., Franca, T. and Calvani, C., 2024. Making wood inspection easier: FTIR spectroscopy and machine learning for Brazilian native commercial wood species identification. RSC Advances, 14, **11**, 7283–7289. https://doi.org/10.1039/D4RA00174E

Joseph, I.V., 2021. Water purification using zeolites prepared from clay and ash-derived waste materials. *PhD Thesis*, Manchester Metropolitan University.

Kannan, N. and Sundaram, M.M., 2001. Kinetics and mechanism of removal of methylene blue by adsorption on various carbons—A comparative study. Dyes and Pigments, 51, 1, 25–40. https://doi.org/10.1016/S0143-7208(01)00056-0

Karume, I., Bbumba, S., Tewolde, S., Mukasa, I.H.Z. and Ntale, M., 2023. Impact of carbonization conditions and adsorbate nature on the performance of activated carbon in water treatment. BMC Chemistry, 17, **1**, 162. https://doi.org/10.1186/s13065-023-01091-1

Khapre, M., Shekhawat, A., Saravanan, D., Pandey, S. and Jugade, R., 2022. Mesoporous Fe–Al-doped cellulose for the efficient removal of reactive dyes. Materials Advances, 3, **7**, 3278–3285. https://doi.org/10.1039/D2MA00146B

Kızıl, Y., Benek, V., Teğin, İ., Önal, Y., Erol, K. and Alacabey, İ., 2024. Reactive Blue 19 adsorption on activated carbon from pumpkin (Cucurbita pepo) seed waste: Kinetic, isotherm and thermodynamic studies. Environmental Research, Engineering and Management, 80, **1**, 7–20.

https://doi.org/10.5755/j01.erem.80.1.34243

Kouhail, M., Elahmadi, Z., Benayada, A. and Dewil, R., 2020. Adsorption of Reactive Dyes and Their Mixtures on Activated Carbon: Kinetic, Equilibrium and Thermodynamic Evaluation. Environmental Protection Engineering, 46, **2**, 5–24. https://doi.org/10.37190/epe200201

Kumar, P.S., et al., 2022. Modeling of Reactive Black 5 azo dye adsorption from aqueous solution on activated carbon prepared from poplar sawdust using response surface methodology. International Journal of Environmental Analytical Chemistry, 102, 18, 6970–6987. https://doi.org/10.1080/03067319.2020.1819991

Kumaravel, S., Geetha, M., Niyitanga, T., Kumar, D.S., Al-Ansari, M.M., Mythili, R., Suganthi, S., Guganathan, L., Murugan, A. and Ragupathy, S., 2024. Preparation and characterization of activated carbon from corn cob by chemical activation and their adsorption of brilliant green dye from wastewater. Process Safety and Environmental Protection, 188, 1338–1345. https://doi.org/10.1016/j.psep.2024.05.127

Kundu, S., Khandaker, T., Anik, M.A.A.M., Hasan, M.K., Dhar, P.K., Dutta, S.K., Latif, M.A. and Hossain, M.S., 2024. A comprehensive review of enhanced CO_2 capture using activated carbon derived from biomass feedstock. RSC Advances, 14, 40, 29693–29736. https://doi.org/10.1039/D4RA04537H

Kyzas, G.Z. and Kostoglou, M., 2014. Green adsorbents for wastewaters: a critical review. Materials, 7, 1, 333–364. https://doi.org/10.3390/ma7010333

Lai, W., Yang, S., Jiang, Y., Zhao, F., Li, Z., Zaman, B., Fayaz, M., Li, X. and Chen, Y., 2020. Artefact peaks of pore size distributions caused by unclosed sorption isotherm and tensile strength effect. Adsorption, 26, 4, 633–645. https://doi.org/10.1007/s10450-020-00228-1

Lawtae, P. and Tangsathitkulchai, C., 2021. The use of high surface area mesoporous-activated carbon from longan seed biomass for increasing capacity and kinetics of methylene blue adsorption from aqueous solution. Molecules, 26, **21**, 6521. https://doi.org/10.3390/molecules26216521

Ledakowicz, S. and Paździor, K., 2021. Recent achievements in dyes removal focused on advanced oxidation processes integrated with biological methods. Molecules, 26, **4**, 870. https://doi.org/10.3390/molecules26040870

Li, G., Iakunkov, A., Boulanger, N., Lazar, O.A., Enachescu, M., Grimm, A. and Talyzin, A.V., 2023. Activated carbons with extremely high surface area produced from cones, bark and wood using the same procedure. RSC Advances, 13, **21**, 14543–14553. https://doi.org/10.1039/D3RA00820G

Li, J., Huang, C.Y. and Li, C.J., 2022. Deoxygenative functionalizations of aldehydes, ketones and carboxylic acids. Angewandte Chemie, 134, **10**, e202112770. https://doi.org/10.1002/ange.202112770

Li, Q., Su, H., Yang, Y., Zhang, J., Xia, C. and Guo, Z., 2023. Adsorption property and mechanism of glutaraldehyde-crosslinked chitosan for removal of 2,4-dichlorophenoxyacetic acid from water. Environmental Science: Water Research & Technology, 9, **1**, 294–307. https://doi.org/10.1039/D2EW00638C

Li, X., Xu, J., Luo, X. and Shi, J., 2022. Efficient adsorption of dyes from aqueous solution using a novel functionalized magnetic biochar: synthesis, kinetics, isotherms, adsorption mechanism, and reusability. Bioresource Technology, 360, 127526. https://doi.org/10.1016/j.biortech.2022.127526

Liu, Y., Chen, J., Duan, D., Zhang, Z., Liu, C., Cai, W. and Zhao, Z., 2024. Environmental impacts and biological technologies toward sustainable treatment of textile dyeing wastewater: a review. Sustainability, 16, **24**, 10867. https://doi.org/10.3390/su162410867

Liu, Z., Fan, W. and Xu, Y., 2024. Synthesis and characterisation of K_2CO_3-activated carbon produced from distilled spent grains for the adsorption of CO_2. Environmental Science and Pollution Research, 31, **23**, 34726–34737. https://doi.org/10.1007/s11356-024-33584-4

Luo, M., Yang, S., Shen, S. and Li, Y., 2020. Adsorption characteristics of oxytetracycline by different fractions of the organic matter from humus soil: insight from internal structure and composition. International Journal of Environmental Research and Public Health, 17, **3**, 914. https://doi.org/10.3390/ijerph17030914

Lykidou, S., Gitsouli, E., Daniilidis, V., Vouvoudi, E. and Nikolaidis, N.F., 2023. Study on the dyeing properties of a novel reactive dye with one vinylsulfone reactive group on cotton substrates before and after its ultrafiltration treatment. Fibers and Polymers, 24, **11**, 3995–4004. https://doi.org/10.1007/s12221-023-00366-7

Mahmood, U., Alkorbi, A.S., Hussain, T., Nazir, A., Qadir, M.B., Khaliq, Z., et al., 2024. Adsorption of lead ions from wastewater using electrospun zeolite/MWCNT nanofibers: kinetics, thermodynamics and modeling study. RSC Advances, 14, **9**, 5959–5974. https://doi.org/10.1039/D3RA07720A

Mamatha, M., 2023. A review on activated carbon: preparation, characterization and applications. *International Journal for Research and Analytical Engineering & Science & Technology (IJRASET)*, 5(4).

Marsh, H., Rodríguez-Reinoso, F., 2006. Activated Carbon. Elsevier, Oxford.

Mosaffa, E., Patel, R.I., Banerjee, A., Basak, B.B. and Oroujzadeh, M., 2024. Comprehensive analysis of cationic dye removal from synthetic and industrial wastewater using a semi-natural curcumin grafted biochar/poly acrylic acid composite hydrogel. RSC Advances, 14, **11**, 7745–7762. https://doi.org/10.1039/D3RA08521J

Obulapuram, P.K., Arfin, T., Mohammad, F., Khiste, S.K., Chavali, M., Albalawi, A.N. and Al-Lohedan, H.A., 2021. Adsorption, equilibrium isotherm, and thermodynamic studies towards the removal of reactive orange 16 dye using Cu(I)-polyaniline composite. Polymers, 13, 20, 3490. https://doi.org/10.3390/polym13203490

Olivito, F., Algieri, V., Jiritano, A., Tallarida, M.A., Tursi, A., Costanzo, P., Maiuolo, L. and De Nino, A., 2021. Cellulose citrate: a convenient and reusable bio-adsorbent for effective removal of methylene blue dye from artificially contaminated water. RSC Advances, 11, 34309–34318. https://doi.org/10.1039/D1RA05464C

Pan, S.Y., Syu, W.J., Chang, T.K. and Lee, C.H., 2020. A multiple model approach for evaluating the performance of time-lapse capsules in trapping heavy metals from water bodies. RSC Advances, 10, **28**, 16490–16501. https://doi.org/10.1039/D0RA03017A

Pérez, N.P., Travieso, J.A.R., Shelton, E.D.E., Pedroso, D.T., Machin, E.B., Tuna, C.E. and Silveira, J.L., 2025. Unlocking the potential of sugarcane bagasse: a comprehensive analysis for advanced energy conversion. Bioresources and Bioprocessing, 12, **1**, 60. https://doi.org/10.1186/s40643-025-00878-5

Petri, E., Heigl, E.M., Fasolini, A., Zeilerbauer, L., Giovannucci, M., Küçükağa, Y., Torri, C., Basile, F. and Soavi, F., 2024. Conversion of biodigestate into activated carbon for electrochemical application: process performance and life cycle assessment. Carbon, 226, 119221. https://doi.org/10.1016/j.carbon.2024.119221

Pieczykolan, B., 2025. Investigation of adsorption kinetics and isotherms of synthetic dyes on biochar derived from post-coagulation sludge. International Journal of Molecular Sciences, 26, **16**, 7912. https://doi.org/10.3390/ijms26167912

Pimentel, C.H., Castro-Agra, R., Freire, M.S., Gómez-Díaz, D. and González-Álvarez, J., 2025. Adsorption of anionic wood dyes on KOH-activated carbons from Pinus radiata sawdust. Biomass Conversion and Biorefinery, 15, 5, 7603–7622. https://doi.org/10.1007/s13399-024-05587-1

Purnomo, A.S., Bahruji, H., Allouss, D., El Alaoui-Elbalrhiti, I., Subagyo, R., Rohmah, A.A. and Prasetyoko, D., 2023. Hectorite-CTAB–alginate composite beads for water treatment: kinetic, isothermal and thermodynamic studies. RSC Advances, 13, **2**, 790–801. https://doi.org/10.1039/D2RA06934B

Rahman, N.U., Ullah, I., Alam, S., Khan, M.S., Shah, L.A., Zekker, I., et al., 2021. Activated Ailanthus altissima sawdust as adsorbent for removal of Acid Yellow 29 from wastewater: kinetics approach. Water, 13, **15**, 2136. https://doi.org/10.3390/w13152136

Sadoun, L., Seffah, K., Benmounah, A., Zerizer, A. and Ghernaout, D., 2023. High-performance raw biosorbent derived from Algerian Zean oak sawdust for removing methylene blue from aqueous environments. Desalination and Water Treatment, 294, 233–246. https://doi.org/10.5004/dwt.2023.29548

Sahmoune, M.N., 2019. Evaluation of thermodynamic parameters for adsorption of heavy metals by green adsorbents. Environmental Chemistry Letters, 17, **2**, 697–704. https://doi.org/10.1007/s10311-018-00819-z

Sahu, S., Bakshi, A., Gupta, M. and Ghosh, N.D., 2020. Adsorption of Reactive Dyes from Aqueous Solution Using Activated Carbon Prepared from Plantain Leaf Sheath Waste. Chemical and Biochemical Engineering Quarterly, 34, **3**, 169–180. https://doi.org/10.15255/CABEQ.2020.1826

Saleem, J., Moghal, Z.K.B., Pradhan, S. and McKay, G., 2024. High-performance activated carbon from coconut shells for dye removal: study of isotherm and thermodynamics. *RSC Advances*, 14, **46**, 33797–33808. https://doi.org/10.1039/D4RA06287F

Sanni, S., Tchakala, I., Kodom, T., Karamoko, B.A., Bawa, L.M. and Holade, Y., 2025. Activated carbons derived from brewing cereal residues and pineapple peelings for removal of Acid Orange 7 (AO7) dye. Molecules, 30, **4,** 881. https://doi.org/10.3390/molecules30040881

Shikuku, V.O. and Mishra, T., 2021. Adsorption isotherm modeling for methylene blue removal onto magnetic kaolinite clay: a comparison of two-parameter isotherms. Applied Water Science, 11, **6**, 103. https://doi.org/10.1007/s13201-021-01440-2

Sirach, R. and Dave, P.N., 2023. Thermal and bisphenol-A adsorption properties of a zinc ferrite/β-cyclodextrin polymer nanocomposite. RSC Advances, 13, **32**, 21991–22006. https://doi.org/10.1039/D3RA03331G

Slama, H.B., Chenari Bouket, A., Pourhassan, Z., Alenezi, F.N., Silini, A., Cherif-Silini, H., et al., 2021. Diversity of synthetic dyes from textile industries, discharge impacts and treatment methods. Applied Sciences, 11, 14, 6255. https://doi.org/10.3390/app11146255

Srivastava, A. and Srivastava, N., 2025. Adsorptive removal of malachite green using fox nutshell activated carbon: adsorption isotherms and kinetic study. *Indian Journal of Chemical Technology (IJCT)*, 32, **2**, 230–240.

Strebel, A., Behringer, M., Hilbig, H., Machner, A. and Helmreich, B., 2024. Anionic azo dyes and their removal from textile wastewater through adsorption by various adsorbents: a critical review. Frontiers in Environmental Engineering, 3, 1347981. https://doi.org/10.3389/fenve.2024.1347981

Teweldebrihan, M.D., Gnaro, M.A. and Dinka, M.O., 2024. The application of magnetite biochar composite derived from Parthenium hysterophorus for the adsorption of methylene blue from aqueous solution. Frontiers in Environmental Science, 12, 1375437. https://doi.org/10.3389/fenvs.2024.1375437

Thamer, B.M., Al-Aizari, F.A. and Abdo, H.S., 2023. Enhanced adsorption of textile dyes by a novel sulfonated activated carbon derived from pomegranate peel waste: isotherm, kinetic and thermodynamic study. Molecules, 28, **23**, 7712. https://doi.org/103390/molecules28237712

Tian, Y., Chen, Q., Yan, C., Deng, H. and He, Y., 2020. Classification of adsorption isotherm curves for shale based on pore structure. Petrophysics, 61, **5**, 417–433. https://doi.org/10.30632/PJV61N5-2020a2

Tichem, T.M., Wang, Y., Gameli, R.B., Mbage, B. and Li, B., 2023. Multicomponent adsorption of pollutants from wastewater using low-cost eco-friendly iron-modified rice husk biochar in the era of green chemistry. Sustainability, 15, **23**, 16348. https://doi.org/10.3390/su152316348

Tran, H.N., 2022. Improper estimation of thermodynamic parameters in adsorption studies with distribution coefficient K_D (q_e/C_e) or Freundlich constant (K_F): Considerations from the derivation of dimensionless thermodynamic equilibrium constant and suggestions. *Adsorption Science & Technology*, 2022, 5553212. https://doi.org/10.1155/2022/5553212

Tsai, C.H., Tsai, W.T. and Kuo, L.A., 2023. Effect of post-washing on textural characteristics of carbon materials derived from pineapple peel biomass. Materials, 16, **24**, 7529. https://doi.org/10.3390/ma16247529

Ullah, N., Ali, Z., Khan, A.S., Adalat, B., Nasrullah, A. and Khan, S.B., 2024. Preparation and dye adsorption properties of activated carbon/clay/sodium alginate composite hydrogel membranes. RSC Advances, 14, **1**, 211–221. https://doi.org/10.1039/D3RA07554K

Ulpathakumbura, S., Marikkar, N. and Jayasinghe, L., 2023. FTIR spectral correlation with alpha-glucosidase inhibitory activities of selected leafy plants extracts. International Journal of Plant Based Pharmaceuticals, 3, **1**, 104–113. https://doi.org/10.29228/ijpbp.22

Vojnović, B., Cetina, M., Franjković, P. and Sutlović, A., 2022. Influence of Initial pH Value on the Adsorption of Reactive Black 5 Dye on Powdered Activated Carbon: Kinetics, Mechanisms, and Thermodynamics. Molecules, 27, **4**, 1349. https://doi.org/10.3390/molecules27041349

Wang, Z., Sun, C., Xu, Q., Zou, X., Cheng, H. and Lu, X., 2022. In situ XRD, Raman characterization, and kinetic study of CO_2 capture by alkali carbonate-doped Na_4SiO_4. Separations, 9, **12**, 428. https://doi.org/10.3390/separations9120428

Wu, F.C., Tseng, R.L. and Juang, R.S., 2009. Initial behavior of intraparticle diffusion model used in the description of adsorption kinetics. Chemical Engineering Journal, 153, 1–3, 1–8. https://doi.org/10.1016/j.cej.2009.04.042

Yadav, M., Singh, N., Annu, Khan, S.A., Raorane, C.J. and Shin, D.K., 2024. Recent advances in utilizing lignocellulosic biomass materials as adsorbents for textile dye removal: a comprehensive review. Polymers, 16, **17**, 2417. https://doi.org/10.3390/polym16172417

Zaidi, R., Khan, S.U., Farooqi, I.H. and Azam, A., 2021. Investigation of kinetics and adsorption isotherm for fluoride removal from aqueous solutions using mesoporous cerium–aluminum binary oxide nanomaterials. RSC Advances, 11, **46**, 28744–28760. https://doi.org/10.1039/D1RA00598G

Zayed, A.M., Metwally, B.S., Masoud, M.A., Mubarak, M.F., Shendy, H., Abdelsatar, M.M., et al., 2023. Efficient dye removal from industrial wastewater using sustainable activated carbon and its polyamide nanocomposite derived from agricultural and industrial wastes in column systems. RSC Advances, 13, **36**, 24887–24898. https://doi.org/10.1039/D3RA03105E

Zhang, L., 2023. Removal of chloride ions from desulfurization wastewater by ZnMgAl-LDHs. Desalination and Water Treatment, 299, 110–117. https://doi.org/10.5004/dwt.2023.29696